photonics

Article

NaGdF$_4$:Yb, Er, Tm Upconversion Nanoparticles for Bioimaging in Shortwave-Infrared Range: Study of Energy Transfer Processes and Composition Optimization

Daria Pominova [1,2], Vera Proydakova [1], Igor Romanishkin [1], Sergei Kuznetsov [1], Kirill Linkov [1], Nataliya Tabachkova [1,3] and Anastasia Ryabova [1,2,*]

[1] Prokhorov General Physics Institute of the Russian Academy of Sciences, 38 Vavilova Str., 119991 Moscow, Russia; pominovadv@nsc.gpi.ru (D.P.); igor.romanishkin@nsc.gpi.ru (I.R.); ntabachkova@misis.ru (N.T.)
[2] National Research Nuclear University MEPHI, 31 Kashirskoe Highway, 115409 Moscow, Russia
[3] Department of Materials Science of Semiconductors and Dielectrics, National University of Science and Technology «MISIS», Leninskiy Prospect, 4, 119049 Moscow, Russia
* Correspondence: nastya.ryabova@nsc.gpi.ru

Abstract: Upconversion nanoparticles are promising for many applications. For triple-doped nanoparticles (NPs), the luminescence intensity shows a non-linear dependence on the rare-earth ion concentration, making it difficult to obtain bright phosphors with high energy output. We investigated the energy transfer processes in β-NaGdF$_4$:Yb-Er-Tm NPs and considered strategies for increasing the thulium luminescence intensity, in particular, the use of core–shell structures. The luminescence spectra were analyzed in the short-wavelength infrared (SWIR) and visible (VIS) regions. The Er^{3+} and Tm^{3+} luminescence lifetimes in the VIS region were measured to study the energy transfer processes between the active ions. The quenching of the Tm^{3+} luminescence in the SWIR region was observed. However, both Er^{3+} and Tm^{3+} luminescence bands were observed in the VIS range. We attribute these effects to energy transfer between Tm^{3+} $^3F_4 \rightarrow {}^3H_6$ and Er^{3+} $^4I_{13/2} \rightarrow {}^4I_{9/2}$, which occurs due to overlap of Er^{3+} and Tm^{3+} luminescence bands, and also to competition between Er^{3+} and Tm^{3+} for energy transfer from Yb^{3+}. For core–shell NPs, when Tm^{3+} and Er^{3+} are separated into adjacent layers, quenching cannot be avoided, likely due to the mutual diffusion of ions during shell synthesis. The most optimal strategy to obtain luminescence in the SWIR range is to use an inert intermediate shell between the layers containing Tm^{3+} and Er^{3+}.

Keywords: bioimaging; short-wavelength infrared region; energy transfer; rare earth ions; upconversion; nanoparticles; solvothermal synthesis technique

Citation: Pominova, D.; Proydakova, V.; Romanishkin, I.; Kuznetsov, S.; Linkov, K.; Tabachkova, N.; Ryabova, A. NaGdF$_4$:Yb, Er, Tm Upconversion Nanoparticles for Bioimaging in Shortwave-Infrared Range: Study of Energy Transfer Processes and Composition Optimization. *Photonics* **2024**, *11*, 38. https://doi.org/10.3390/photonics11010038

Received: 9 November 2023
Revised: 22 December 2023
Accepted: 27 December 2023
Published: 30 December 2023

1. Introduction

In recent years, upconversion nanoparticles (UCNPs), which produce higher-energy VIS or near-infrared (NIR) luminescence when excited with low-energy NIR light, have been extensively investigated. Due to their unique characteristics [1–3] such as very high photostability, absence of photo blinking, long luminescence lifetimes, narrow emission peaks with large shifts relative to the excitation wavelength, low toxicity, low imaging background, and functional multimodality, they have been used in a variety of applications, including bioimaging [4,5], solar cell enhancement [6,7], chemical and biosensing [8–11], contactless thermometry at the nanoscale [12,13], cancer therapy [14,15], and anti-counterfeiting [16]. UCNPs are highly attractive for biosensing and bioimaging applications due to their ability to be excited by NIR radiation, which results in lower photo-damage and autofluorescence, as well as deeper penetration into biological tissues due to lower absorption and scattering [17].

UCNPs typically consist of an inert matrix doped with two types of active ions: sensitizers and acceptors. The sensitizer absorbs exciting NIR excitation and non-radiatively transfers energy to an acceptor that luminesces in the visible or NIR range [18]. UCNPs doped with Yb^{3+}-Tm^{3+} are especially promising because they can could convert NIR excitation to NIR luminescence [19–21] and operate within the biological tissue transparency window at wavelengths between 650 nm and 950 nm. However, this range is not optimal due to tissue autofluorescence and background noise, which limit the tissue penetration depth to 1–2 cm [22]. In 2003, it was demonstrated that fluorescence imaging can be significantly improved in depth and sensitivity by using fluorophores that emit light in the short-wavelength infrared (SWIR) at 1320 nm. This also provides excellent contrast and a high signal-to-noise ratio for the resulting luminescence images [23]. Nowadays, there is a growing interest in bioimaging in the second (1000–1350 nm) and third (1500–1800 nm) biological windows [24–27]. However, the lack of biocompatible fluorescent probes limits the use of this highly sensitive spectral range for in vivo imaging. One of them are UCNPs doped with rare-earth ions, which can be excited through multiple electron states and produce luminescence bands in a wide range of the visible (VIS), NIR, and SWIR spectra [28,29]. A significant number of publications are devoted to the study of nanoparticles (NPs) with triple doping, which could be used for multimodal bioimaging with subsequent control of temperature, microenvironment, or probing depth [30–38]. Doping with multiple active ions allows for the production of multicolor luminescence with controllable bands upon single wavelength excitation [39–42].

For biomedical applications, it is very important to achieve high intensity of upconversion luminescence. The luminescent properties of UCNPs strongly depend on many factors, including their matrix and doping ions concentration, particle size, shape, phase and morphology, nanostructure design (such as core−shell parameters), surface ligands, and excitation characteristics (including pumping power density and beam profile) [43–47]. The choice of host material is crucial for achieving high upconversion luminescence intensity. The hexagonal $NaYF_4$ reported to be the most effective matrix due to its low phonon energy [48–51]. The hexagonal phase NaGdF4, which was studied in this work, possesses even lower values of phonon energy [52].

Many papers are devoted to optimizing of the composition and structure of UCNPs to achieve intense upconversion luminescence in the VIS and NIR ranges [53], but the luminescence in the SWIR range has not been thoroughly studied yet. The study of energy transfer processes in NPs with triple doping is of great importance for optimizing the dopant concentration and obtaining SWIR phosphors with high quantum efficiency. The development of SWIR-based luminescent markers with high luminescence intensity under infrared excitation is one of the urgent tasks today. This study focuses on synthesizing β-$NaGdF_4$ NPs doped with rare-earth ions Yb^{3+}, Er^{3+}, and Tm^{3+}, investigating their luminescence characteristics and effect of the shell on the luminescence intensity and energy transfer processes between the rare-earth ions.

Er^{3+} and Tm^{3+} ions are promising for obtaining multicolor luminescence in various spectral ranges because their matching energy levels enable several resonant and non-resonant energy transfers and corresponding spectral tuning. To control the luminescence spectrum, it is necessary to optimize the interactions between ions in such a way that certain transitions are stimulated or suppressed [54]. The successful modulation of the VIS Er^{3+} emission for the Er^{3+}–Tm^{3+} ion pair has been realized. After the introduction of Tm^{3+}, the green emission of Er^{3+} ($^2H_{11/2} \rightarrow {}^4I_{15/2}$, $^4S_{3/2} \rightarrow {}^4I_{15/2}$) decreased, while the red emission ($^4F_{9/2} \rightarrow {}^4I_{15/2}$) increased due to the presence of the cross-relaxation process $^3F_4$ (Tm^{3+}) + $^4I_{11/2}$ (Er^{3+}) $\rightarrow$ $^3H_6$ (Tm^{3+}) + $^4F_{9/2}$ (Er^{3+}) [55]. This hypothesis was confirmed by a kinetic model that provided microscopic insight into the energy transfer pathways leading to spectrally pure emission in multi-doped UCNPs [56,57].

To obtain intense luminescence, it is also important to reduce quenching on high energy surface oscillators [58]. This can be achieved by using core–shell or complex core–multishell structures [20,59]. Adding an intermediate shell between the core and second shell, doped with different active ions, prevents direct chemical and energy transfer interactions between the active ions. This results in multicolor luminescence with high intensity [58,60]. However, it has been shown that active ions in different shells can interact [61]; therefore, determining the optimal shell thickness and composition is usually a complex issue. Efficient energy transfer between ions in adjacent shells has also been reported in the literature [62].

In this article, we investigated how the processes of energy transfer between Er^{3+}–Tm^{3+} ions in triple-doped β-$NaGdF_4$:Yb-Er-Tm NPs affect the luminescence in the SWIR range. Various strategies to increase the intensity of thulium luminescence are also considered, including the use of core–shell structures for the separation of active ions.

2. Materials and Methods

2.1. Synthesis and Characterization of Yb, Er, and Tm Doped β-$NaGdF_4$ NPs

The solvothermal technique was used to synthesize oleate-stabilized β-$NaGdF_4$: Yb(30.0 mol.%):Tm(0.5 mol.%) NPs, β-$NaGdF_4$:Yb(20.0 mol.%):Tm(2.0 mol.%) and Yb-Er-Tm tri-doped β-$NaGdF_4$ NPs as described in [42,63]. No additional purification procedures were employed for the chemicals used. Ytterbium, thulium, and gadolinium acetates (99.99%, LANHIT, Russia) were added to a 500 mL three-necked flask with a reflux condenser. Then, oleic acid (Chimmed, purity) and octadecene-1 (90%, tech Acros Organic) were added. The solution was stirred and heated to 140 °C under argon atmosphere (4.8 purity) for 30 min to form the Ln(oleate)3 complex and to remove the water and acetic acid under vacuum. The temperature was then lowered to room temperature, and ammonium fluoride (NH_4F) (purity, Chimmed, Russia) and sodium hydroxide (NaOH) (Chimmed, chemical purity) dissolved in the methanol (chemical purity, Chimmed, Russia) were added to the reaction flask with the corresponding oleates. The resulting solution was stirred at 50 °C for 1 h. The solution was then slowly heated to 70 °C to remove methanol under vacuum. After removal of methanol, the solution was heated to 300 °C under argon atmosphere and kept in such conditions for 1.5 h. The sediment of NPs was obtained by centrifugation (6500 rpm, 5 min). The resulting NPs were dispersed in chloroform and washed with alcohol. Part of the prepared NPs was dispersed in cyclohexane for core–shell particle preparation.

To synthesize core–shell NPs, lanthanide acetates were added to a 500 mL three-necked flask with a reflux condenser in appropriate proportions, followed by addition of oleic acid and octadecene-1. The solution was stirred and heated to 140 °C under argon atmosphere for 30 min to form the Ln(oleate)3 complex, and to remove the water and acetic acid under vacuum. The solution was cooled to room temperature before adding the core NPs in cyclohexane and NH_4F with NaOH dissolved in methanol to the reaction flask. The resulting mixture was stirred at 50 °C for 1 h, followed by slow heating to 70 °C to remove methanol and cyclohexane under vacuum. After the removal of methanol, the solution was heated to 310 °C under argon atmosphere and kept in such conditions for 1.5 h. The sediment of NPs was obtained by centrifugation. The resulting NPs were dissolved in chloroform and washed with alcohol.

The determination of the phase composition of the synthesized samples was performed by X-ray powder diffraction (XRD) technique (D8 Bruker® Advance diffractometer with CuKα radiation, Bruker, Karlsruhe, Germany). The lattice parameters and coherent scattering region were calculated using TOPAS v.4.2 software. Particle size and morphology were analyzed by transmission electron microscopy (TEM, Jeol JEM-2100, Jeol, Tokyo, Japan) using ImageJ v.1.53e software.

2.2. Spectroscopic Study of Yb, Er, and Tm Doped β-$NaGdF_4$ NPs in VIS and SWIR Ranges

The study involved measuring luminescence spectra in the VIS and SWIR ranges, as well as luminescence lifetime. Luminescence excitation was carried out using a 980 nm wavelength laser (Biospec, Moscow, Russia). The output power from the optical fiber was measured using a PM100D power meter equipped with an S142C integrating sphere (Thorlabs, Newton, NJ, USA). The laser irradiation was focused onto the sample in a spot with 1 cm^2 area. The pumping power density was estimated to be 1 W/cm^2. Scattered laser radiation and upconversion luminescence were collected by the fiber and delivered to the spectrometer.

Luminescence spectra in the VIS spectral range were measured using a fiber-optic spectrometer LESA-01 (Biospec, Moscow, Russia). To suppress radiation with wavelengths above 900 nm and to record the upconversion luminescence spectrum in the VIS range, the FESH900 interference filter (Thorlabs, USA) was used.

The luminescence spectra in the 1000–1700 nm region were measured with a fiber-optic spectrometer DWARF-Star (StellarNet, Tampa, FL, USA). To suppress radiation with wavelengths below 1050 nm and to record the luminescence spectrum in the SWIR range, the FELH1050 interference filter (Thorlabs, Newton, NJ, USA) was used.

Upconversion luminescence decay kinetics were measured using a C9300-508 streak camera with a C10627-13 streak scope (Hamamatsu, Hamamatsu-city, Japan). The samples were illuminated with pulsed laser radiation at a wavelength of 980 nm. The luminescence signal was recorded using a Hamamatsu streak camera in combination with a fiber-optic light delivery system. The pulse duration was 8 ms with a repetition rate of 100 Hz. The sweep time was 2 ms, starting 0.1 ms before the laser pulse end. The detected luminescence signal was divided into green (transitions $^2H_{11/2}$, $^4S_{3/2} \rightarrow {}^4I_{15/2}$) and red (transitions $^4F_{9/2} \rightarrow {}^4I_{15/2}$ Er^{3+} and $^1G_4 \rightarrow {}^3F_4$ Tm^{3+}) bands. An exponential fit was used to calculate the luminescence lifetime for each band.

3. Results and Discussion

3.1. Synthesis and Characterization of Yb, Er, and Tm Doped β-NaGdF$_4$ NPs

The β-$NaGdF_4$ NPs were synthesized with tri-doping of rare earth ions Yb^{3+}, Er^{3+}, and Tm^{3+} at Yb:Er:Tm ratios of 10:1:0.5 and 10:1:1. Also during the step-by-step synthesis, a series of core–shell samples were obtained: (1) tri-doped with Yb^{3+}, Er^{3+}, and Tm^{3+} rare-earth ions core with Yb:Er:Tm ratio equal to 10:1:0.5 and 10:1:1 covered with inert $NaYF_4$ shell; (2) $NaGdF_4$:Yb-Er core covered with first $NaGdF_4$:Yb-Tm shell, covered with inert $NaYF_4$ shell; (3) $NaGdF_4$:Yb-Tm core covered with first shell $NaGdF_4$:Yb-Er, covered with inert shell $NaYF_4$; and (4) $NaGdF_4$:Yb-Tm core covered with first inert $NaYF_4$ shell (intermediate shell), covered with $NaGdF_4$:Yb-Er shell, covered with second inert $NaYF_4$ shell. The doping concentration ratios of Yb:Tm and Yb:Er were chosen to be 30:0.5 and 20:2, respectively, according to the literature data and our previous study [64,65].

3.1.1. X-ray Powder Diffraction Results

The diffraction patterns of synthesized β-$NaGdF_4$:Yb-Tm(30:0.5), β-$NaGdF_4$:Yb-Tm (30:0.5)@$NaYF_4$, β-$NaGdF_4$:Yb-Tm(30:0.5)@$NaYF_4$@$NaGdF_4$:Yb-Er(20:2), β-$NaGdF_4$:$NaGdF_4$: Yb-Tm(30:0.5)@$NaYF_4$@$NaGdF_4$:Yb-Er(20:2)@$NaYF_4$ samples are shown in Figures 1–3.

Comparison of the X-ray diffraction patterns with JCPDS 27-0699 (a = 6.020 Å, c = 3.601 Å) for β-$NaGdF_4$ and JCPDS 00-016-0334 (a = 5.96 Å, c = 3.53 Å) for β-$NaYF_4$ did not reveal any additional peaks. This indicates that single-phase samples with low-temperature hexagonal phase were synthesized. The calculated lattice parameters are presented in Table 1.

The lattice parameters for samples with the outer shell based on β-$NaGdF_4$ are similar. After synthesizing the $NaYF_4$ shell, a decrease in lattice parameters was observed in the following samples: β-$NaGdF_4$:Yb-Tm(30:0.5)@$NaGdF_4$:Yb-Er(20:2)@$NaYF_4$, β-$NaGdF_4$:Yb-Tm(30:0.5)@$NaYF_4$, β-$NaGdF_4$:Yb-Tm(30:0.5)@$NaYF_4$@$NaGdF_4$:Yb-Er(20:2)@$NaYF_4$, and β-$NaGdF_4$:Yb-Er(20:2)@$NaGdF_4$:Yb-Tm(30:0.5)@$NaYF_4$. This effect could be attributed to the smaller size of yttrium cations compared to gadolinium cations [66]. The analysis of lattice parameters shows that the chemical composition of the outer shell has a strong effect on cell parameters. Despite the different particle size, the lattice parameters for the β-$NaGdF_4$:Yb-Tm(30:0.5)@$NaGdF_4$:Yb-Er(20:2)@$NaYF_4$ and β-$NaGdF_4$:Yb-Tm(30:0.5)@$NaYF_4$ samples are similar due to the same chemical composition of the outer shell.

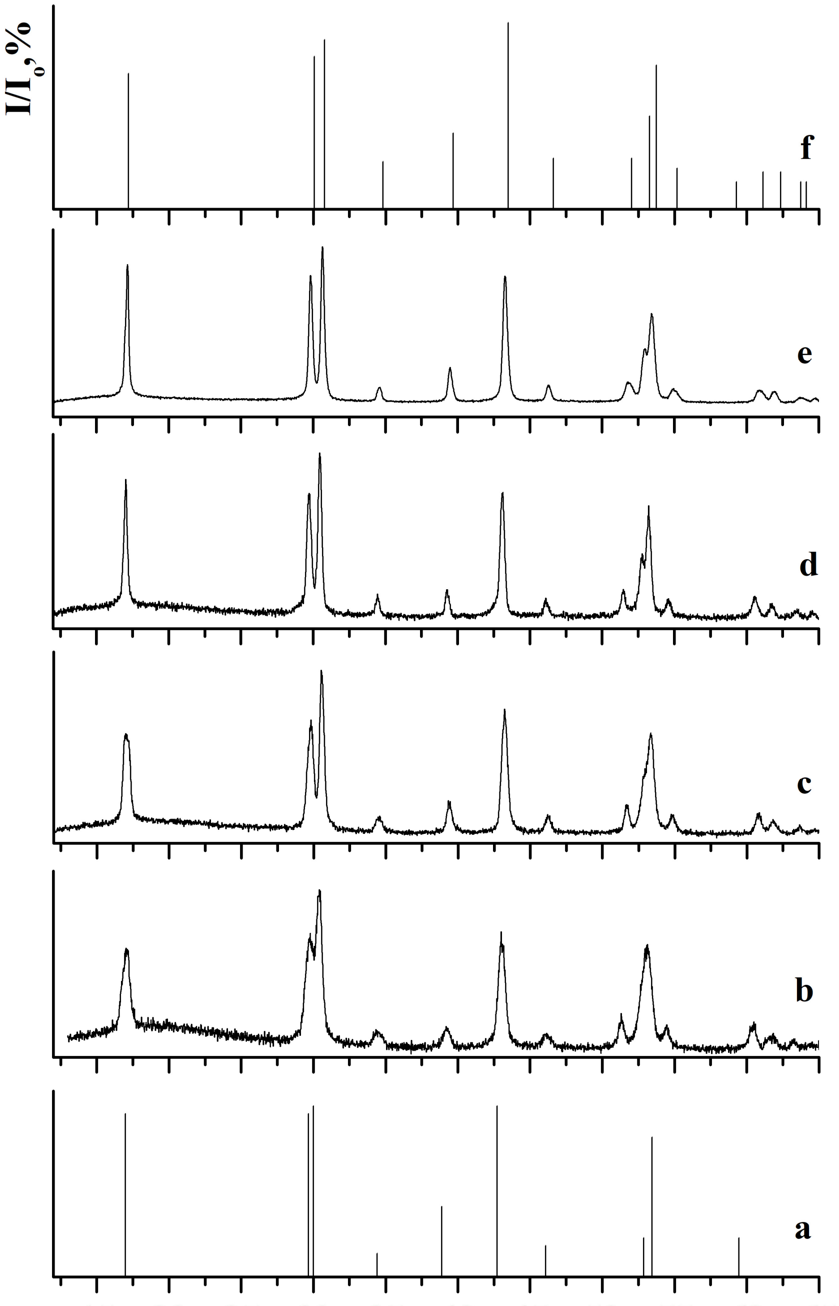

Figure 1. X-ray diffraction pattern of the samples: (**a**) JCPDS 27-0699 of β-$NaGdF_4$, (**b**) β-$NaGdF_4$:Yb-Tm, (**c**) β-$NaGdF_4$:Yb-Tm@$NaYF_4$, (**d**) β-$NaGdF_4$:Yb-Tm@$NaYF_4$@$NaGdF_4$:Yb-Er, (**e**) β-$NaGdF_4$:Yb-Tm@$NaYF_4$@$NaGdF_4$:Yb-Er@$NaYF_4$, and (**f**) JCPDS 00-016-0334 of β-$NaYF_4$.

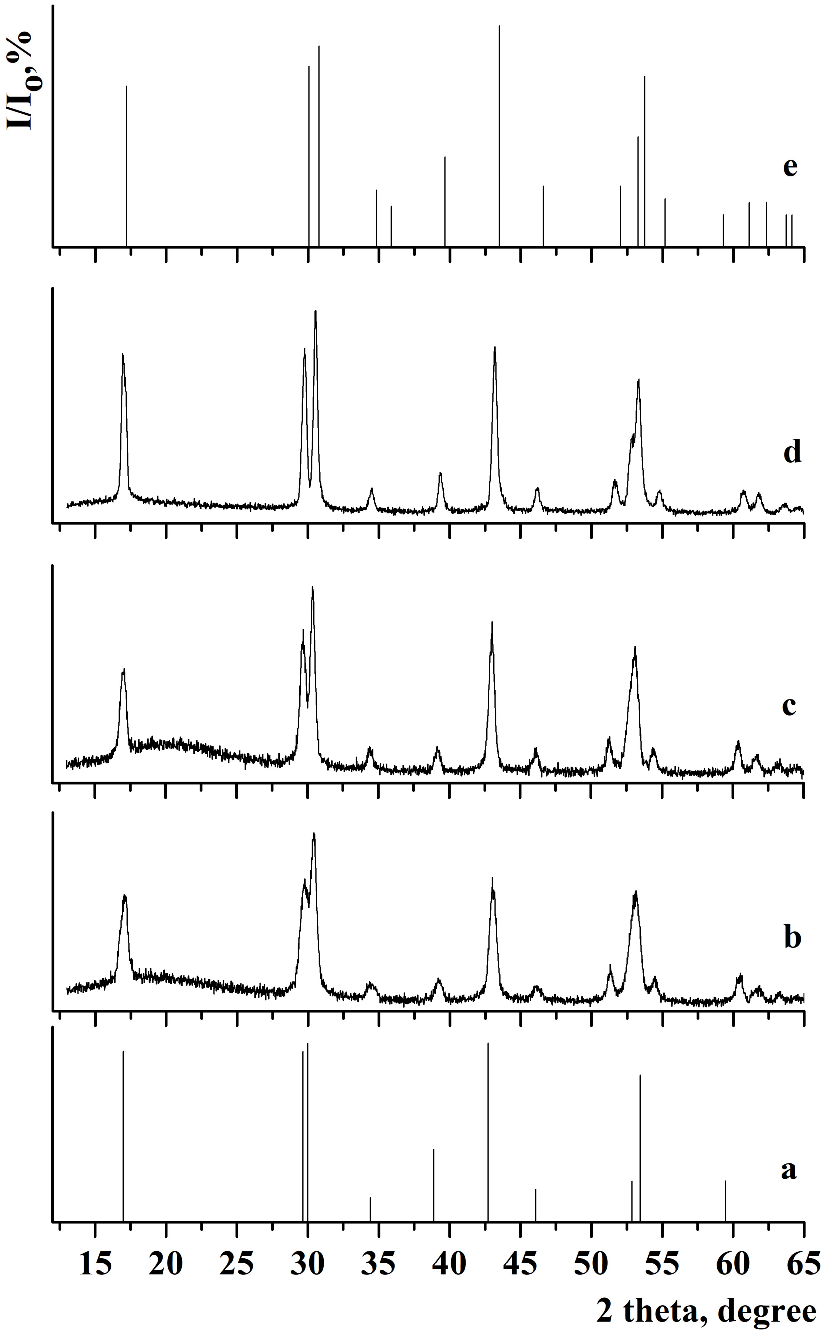

Figure 2. X-ray diffraction pattern of the samples: (**a**) JCPDS 27-0699 of β-$NaGdF_4$, (**b**) β-$NaGdF_4$:Yb-Tm, (**c**) β-$NaGdF_4$:Yb-Tm@$NaGdF_4$:Yb-Er, (**d**) β-$NaGdF_4$:Yb-Tm@$NaGdF_4$:Yb-Er@$NaYF_4$, and (**e**) JCPDS 00-016-0334 of β-$NaYF_4$.

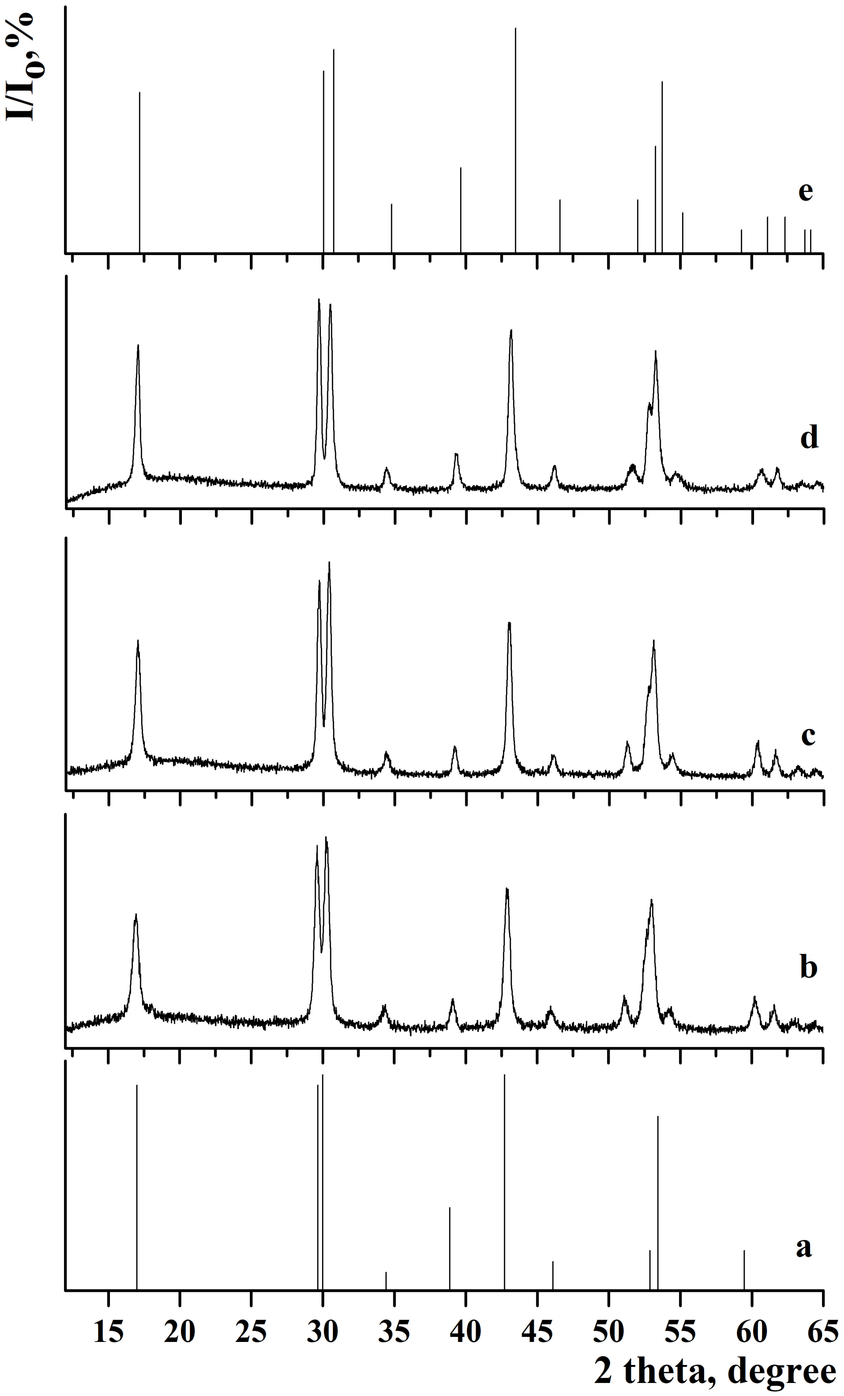

Figure 3. X-ray diffraction pattern of the samples: (**a**) JCPDS 27-0699 of β-$NaGdF_4$, (**b**) β-$NaGdF_4$:Yb-Er, (**c**) β-$NaGdF_4$:Yb-Er@$NaGdF_4$:Yb-Tm, (**d**) β-$NaGdF_4$:Yb-Tm@$NaGdF_4$:Yb-Er@$NaYF_4$, and (**e**) JCPDS 00-016-0334 of β-$NaYF_4$.

Table 1. Lattice parameters, unit cell volume, and coherent scattering regions (D) for samples based on β-$NaGdF_4$: Yb-Tm and β-$NaGdF_4$:Yb-Er core with multishell architecture. ΔD indicates the coherent scattering regions resizing after the next shell growing.

Composition	T, °C	Lattice Parameters, Å^3	Unit Cell Volume, Å	D (nm)	ΔD, nm
β-$NaGdF_4$:Yb-Tm(30:0.5)	300	a = 6.0123 (8) c = 3.5623 (5)	111.51 (4)	13.9 (4)	---
β-$NaGdF_4$:Yb-Tm(30:0.5)@ $NaGdF_4$:Yb-Er(20:2)	310	a = 6.0179 (7) c = 3.5643 (5)	111.79 (3)	17.1 (5)	3.2
β-$NaGdF_4$:Yb-Tm(30:0.5)@ $NaGdF_4$:Yb-Er(20:2)@ $NaYF_4$	310	a = 6.0016 (4) c = 3.5377 (2)	110.35 (2)	23.5 (6)	6.4
β-$NaGdF_4$:Yb-Tm(30:0.5)@ $NaYF_4$	310	a = 5.9997 (4) c = 3.5366 (3)	110.25 (2)	16.7 (3)	2.8
β-$NaGdF_4$:Yb-Tm(30:0.5)@ $NaYF_4$@ $NaGdF_4$:Yb-Er(20:2)	310	a = 6.0113 (4) c = 3.5508 (3)	111.12 (2)	26.5 (4)	9.8
β-$NaGdF_4$:Yb-Tm(30:0.5)@ $NaYF_4$@ $NaGdF_4$:Yb-Er(20:2)@ $NaYF_4$	310	a = 5.9973 (2) c = 3.5315 (1)	110.03 (1)	33.2 (4)	6.7
β-$NaGdF_4$:Yb-Er(20:2)	300	a = 6.0453 (7) c = 3.5985 (5)	113.89 (1)	11.9 (1)	---
β-$NaGdF_4$:Yb-Er(20:2)@ $NaGdF_4$:Yb-Tm(30:0.5)	310	a = 6.0041 (5) c = 3.5586 (2)	111.09 (2)	18 (1)	6.1
β-$NaGdF_4$:Yb-Er(20:2)@ $NaGdF_4$:Yb-Tm(30:0.5)@ $NaYF_4$	310	a = 5.9868 (3) c = 3.5388 (2)	109.85 (1)	22.7 (1)	4.7

The analysis of the samples with $NaYF_4$ shell has shown that the coherent scattering regions resizing after the next shell growth were 6.4 and 6.7 nm in the case of shell growing on β-$NaGdF_4$:Yb-Er (for β-$NaGdF_4$:Yb-Tm(30:0.5)@$NaGdF_4$:Yb-Er(20:2)@$NaYF_4$ and β-$NaGdF_4$:Yb-Tm(30:0.5)@$NaYF_4$@$NaGdF_4$:Yb-Er(20:2)@$NaYF_4$ samples). For $NaYF_4$ grown on β-$NaGdF_4$:Yb-Tm, the sizes of the scattering regions were smaller after the next shell growing, measuring 2.8 and 4.7 nm for the β-$NaGdF_4$:Yb-Tm(30:0.5)@$NaYF_4$ and β-$NaGdF_4$:Yb-Er(20:2)@$NaGdF_4$:Yb-Tm(30:0.5)@$NaYF_4$ samples, respectively.

The coherent scattering region increased in size after the synthesis of each subsequent shell, reaching a maximum value for the $NaGdF_4$:Yb-Tm(30:0.5)@ $NaYF_4$@$NaGdF_4$:Yb-Er(20:2)@$NaYF_4$ sample. This suggests that during the shell synthesis, particle growth occurred through classical crystallization mechanism, where the initial core reacted with appropriate oleates, NaOH and NH_4F from the liquid medium. Finally, the defectiveness of the core surface decreases, the crystallinity of the nanoparticle improves, and the coherent scattering region increases.

3.1.2. Transmission Electron Microscopy Results

The size of the particles was also determined by TEM images, as shown in Figure 4.

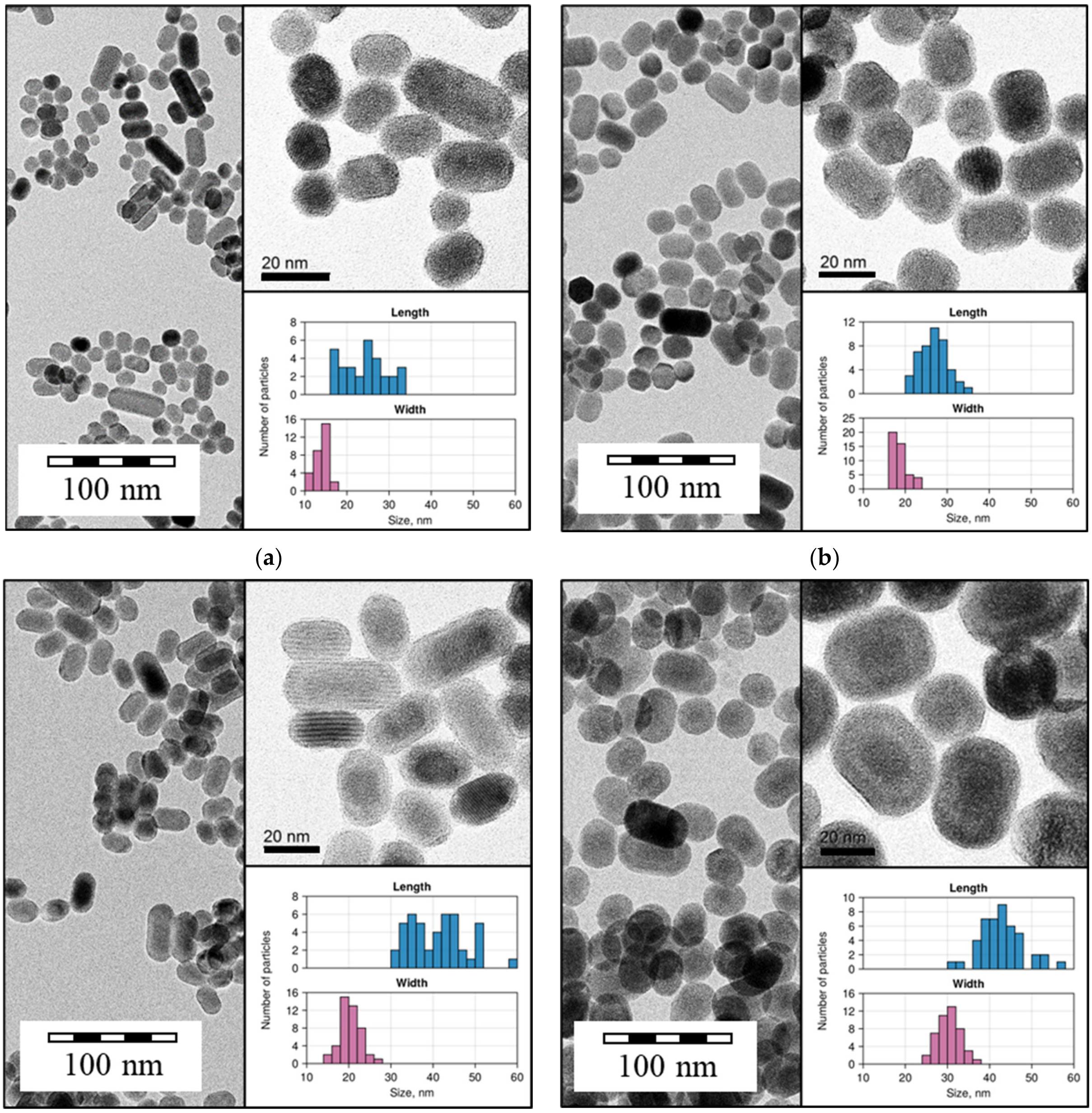

(**a**) (**b**)

(**c**) (**d**)

Figure 4. Micrographs obtained by TEM for (**a**) β-$NaGdF_4$:Yb-Tm(30:0.5); (**b**) β-$NaGdF_4$:Yb-Tm(30:0.5)@$NaGdF_4$:Yb-Er(20:2); (**c**) β-$NaGdF_4$:Yb-Tm(30:0.5)@$NaYF_4$; and (**d**) β-$NaGdF_4$:Yb-Tm(30:0.5)@ $NaYF_4$@$NaGdF_4$:Yb-Er(20:2). Inset: magnified TEM images with adjusted contrast; size distribution histograms for length and width.

According to the TEM data, the samples consisted of particles with semi-spherical morphology. The core-only β-$NaGdF_4$:Yb-Tm(30:0.5) NPs ranged in size from 15 to 40 nm. The increase in particle size was observed after shell synthesis for both $NaGdF_4$:Yb-Er(20:2) and $NaYF_4$ shell; the shell thickness was about 5 nm.

The $NaYF_4$ shell was clearly distinguishable by TEM, in contrast to $NaGdF_4$:Yb-Er, which may be due to the difference in atomic number of yttrium and gadolinium. TEM images revealed the core–shell architecture of $NaGdF_4$:Yb-Tm(30:0.5)@$NaYF_4$@$NaGdF_4$:Yb-Er(20:2) NPs.

3.2. Spectroscopic Study Results

3.2.1. Luminescence Spectra in VIS and SWIR Ranges Analysis

The luminescence spectra, measured in the SWIR range for Yb-Er-Tm tri-doped β-$NaGdF_4$, are presented in Figure 5a. The synthesized tri-doped NPs exhibited 1050 nm ($^2F_{5/2} \rightarrow {}^2F_{7/2}$ Yb^{3+}) and 1540 nm ($^4I_{15/2} \rightarrow {}^4I_{13/2}$ Er^{3+}) luminescence bands in the SWIR range.

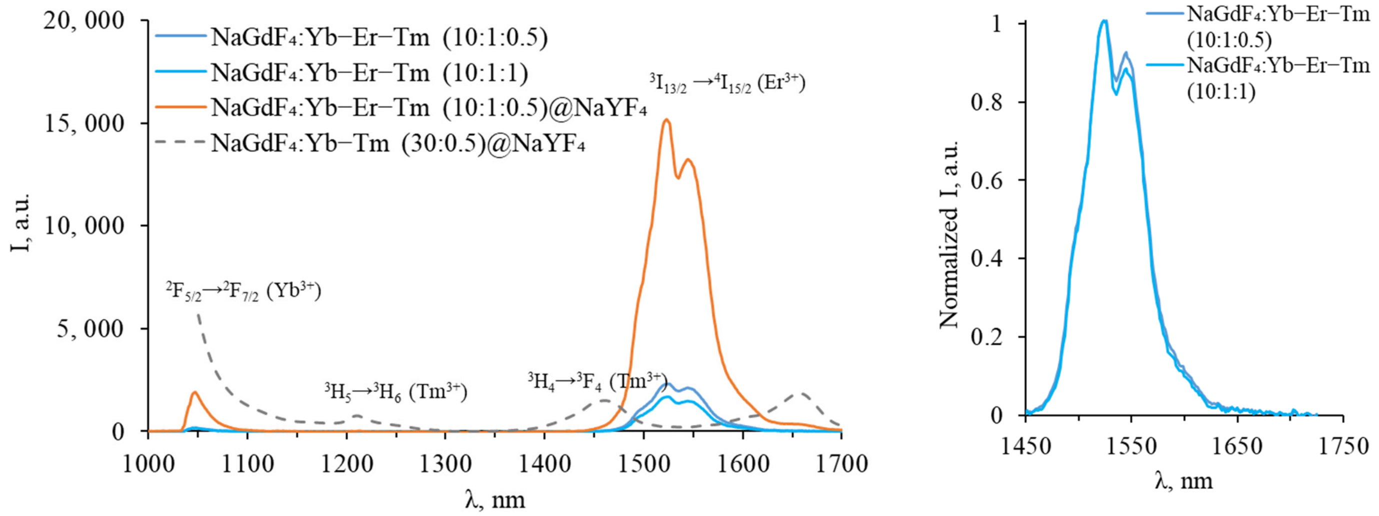

(**a**) (**b**)

Figure 5. (**a**) Luminescence spectra of Yb-Er-Tm tri-doped β-$NaGdF_4$ in the SWIR range; (**b**) same spectra normalized to maximum.

As can be seen from the obtained spectra, no characteristic Tm^{3+} luminescence peaks were observed in the SWIR range for tri-doped NPs. The luminescence bands corresponding to $^3H_4 \rightarrow {}^3H_6$ and $^3F_4 \rightarrow {}^3H_6$ Tm^{3+} transitions (near 1450 nm, and 1650–2000 nm) are absent in the spectra of tri-doped NPs. A two-fold increase in the Tm^{3+} concentration (up to 1%) did not significantly change the shape of the luminescence spectrum. As shown in Figure 4b, only a small decrease in the long-wavelength part of the Er^{3+} emission peak was observed, which could be attributed to energy transfer from Er^{3+} $^4I_{13/2}$ to Tm^{3+} $^3F_4$ or reabsorption of part of the Er^{3+} luminescence by Tm^{3+} ions. The integral Er^{3+} luminescence intensity at 1540 nm wavelength also decreases due to competition between Er^{3+} and Tm^{3+} for energy transfer from Yb^{3+}. After the synthesis of the inert $NaYF_4$ shell, the emission intensity increases dramatically, indicating that the shell separates activators from quenchers and defects on the NPs surface.

To confirm the presence of Tm^{3+} in the NPs composition, we measured the upconversion luminescence spectra of tri-doped NPs in the VIS range, as shown in Figure 6.

The spectra in the VIS range exhibit bands characteristic of both Er^{3+} and Tm^{3+}, confirming the successful doping of the studied NPs with Tm^{3+}. Since Yb^{3+}-Er^{3+} energy transfer is resonant, while Yb^{3+}-Tm^{3+} energy transfer is non-resonant, the transfer to Er^{3+} is more likely. This is the reason for the absence of blue thulium luminescence, which requires at least three energy transfers. However, energy transfer to Tm^{3+} does occur, as evidenced by the presence of a luminescence peak at 800 nm, corresponding to the $^3H_4 \rightarrow {}^3H_6$ transition of thulium. The intensity of thulium luminescence at 800 nm wavelength decreases with an increase in the thulium concentration from 0.5 to 1.0%, which may be due to the cross-relaxation process Tm^{3+}-Tm^{3+}: $^3H_4 \rightarrow {}^3F_4$ and $^3H_6 \rightarrow {}^3F_4$, resulting in a decrease in the population of the $^3H_4$ state, as shown in Figure 7.

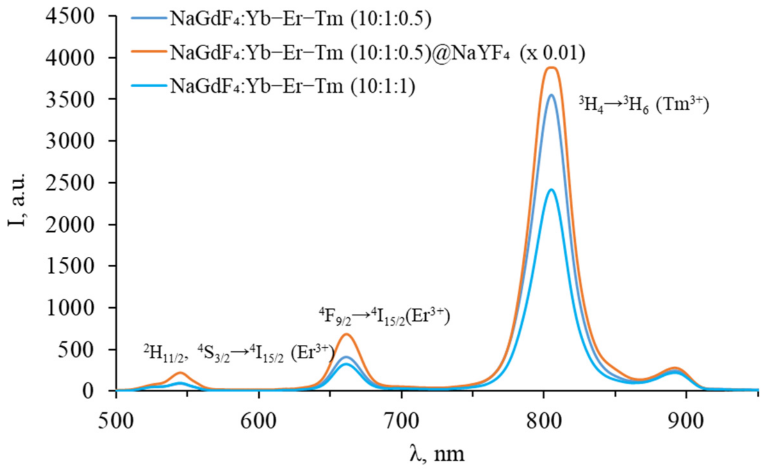

Figure 6. Luminescence spectra of Yb-Er-Tm tri-doped β-$NaGdF_4$ in the VIS range.

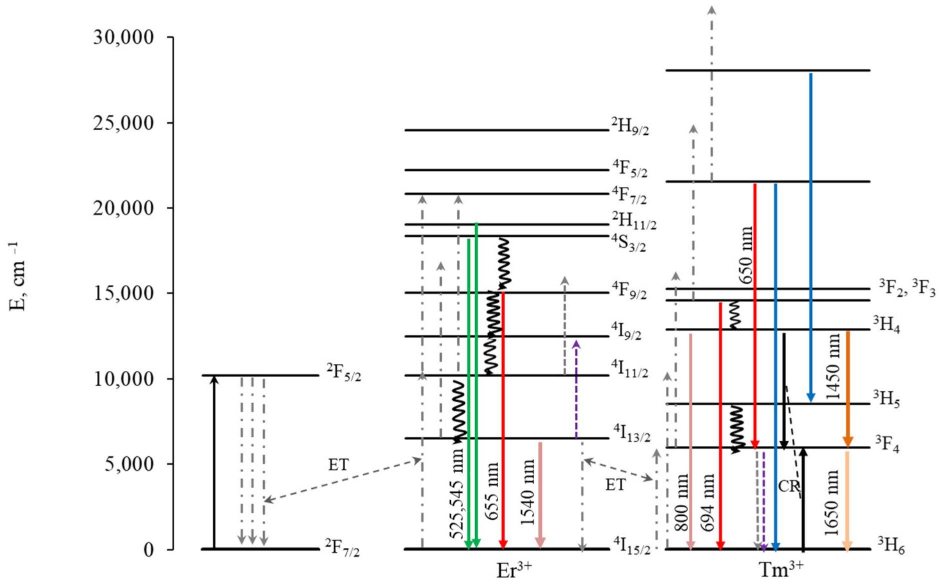

Figure 7. Energy level diagram for Yb-Er-Tm with schematic representation of energy transfer processes.

In contrast to Er-Tm doping, an increase in the thulium concentration leads to a decrease in the red luminescence intensity of erbium for triple doping with Yb-Er-Tm. The increase in red luminescence for Er-Tm doping has been explained in the literature by the $^3F_4$ (Tm^{3+}) + $^4I_{11/2}$ (Er^{3+}) → $^3H_6$ (Tm^{3+}) + $^4F_{9/2}$ (Er^{3+}) cross-relaxation process [55–57]. We assume that in our case there is a cross-relaxation between Tm^{3+} $^3F_4 \rightarrow ^3H_6$ and Er^{3+} $^4I_{13/2} \rightarrow ^4I_{9/2}$, resulting in a decrease in the population of the $^4I_{13/2}$ level. Energy transfer from Yb^{3+} to $^4I_{13/2}$ leads to the population of $^4F_{9/2}$, which causes the red luminescence of erbium. The population of thulium $^3F_4$, which participates in the population of $^3H_4$ during energy transfer from Yb^{3+}, also decreases, which can lead to a decrease in the intensity of luminescence from $^3H_4$ along with cross-relaxation Tm^{3+}-Tm^{3+} $^3H_4 \rightarrow ^3F_4$ and $^3H_6 \rightarrow ^3F_4$, and a decrease in the luminescence of thulium in the SWIR range from the $^3H_4$ level, which occurs between 1600 and 2000 nm. Luminescence in the SWIR range during the $^3H_4 \rightarrow ^3F_4$ transition is less likely than luminescence at 800 nm during the $^3H_4 \rightarrow ^3H_6$ transition and is therefore not observed at low concentrations.

Increasing the thulium concentration does not lead to an increase in this peak due to Tm^{3+}-Tm^{3+}: $^3H_4 \rightarrow ^3F_4$ and $^3H_6 \rightarrow ^3F_4$ cross-relaxation. As a result, Tm^{3+} demonstrated weak luminescence in the SWIR range, making it difficult to distinguish between Tm^{3+} and Er^{3+} luminescence peaks. To prevent energy transfer between Tm^{3+} and Er^{3+}, core–shell

NPs were synthesized, in which Er^{3+} and Tm^{3+} are located in different layers. Spectra in the SWIR and in the VIS ranges recorded for NPs with an Er^{3+} doped core coated with a Tm^{3+} doped shell are shown in Figures 8 and 9.

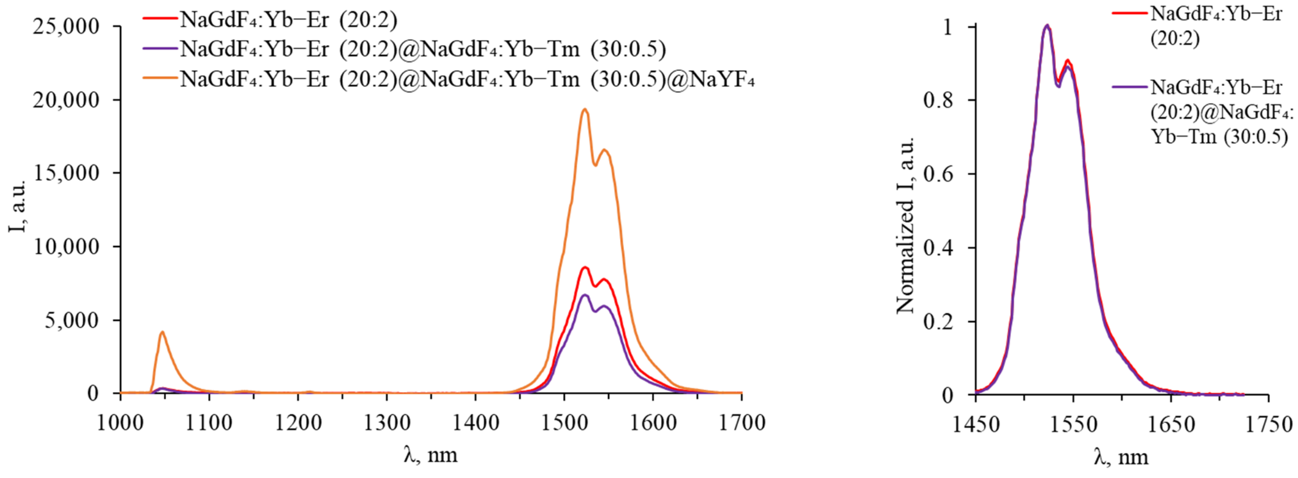

(**a**) (**b**)

Figure 8. (**a**) Luminescence spectra of core–shell β-$NaGdF_4$ ($NaGdF_4$:Yb-Er core covered with first $NaGdF_4$:Yb-Tm shell, covered with inert $NaYF_4$ shell) in SWIR range; (**b**) same spectra normalized to maximum.

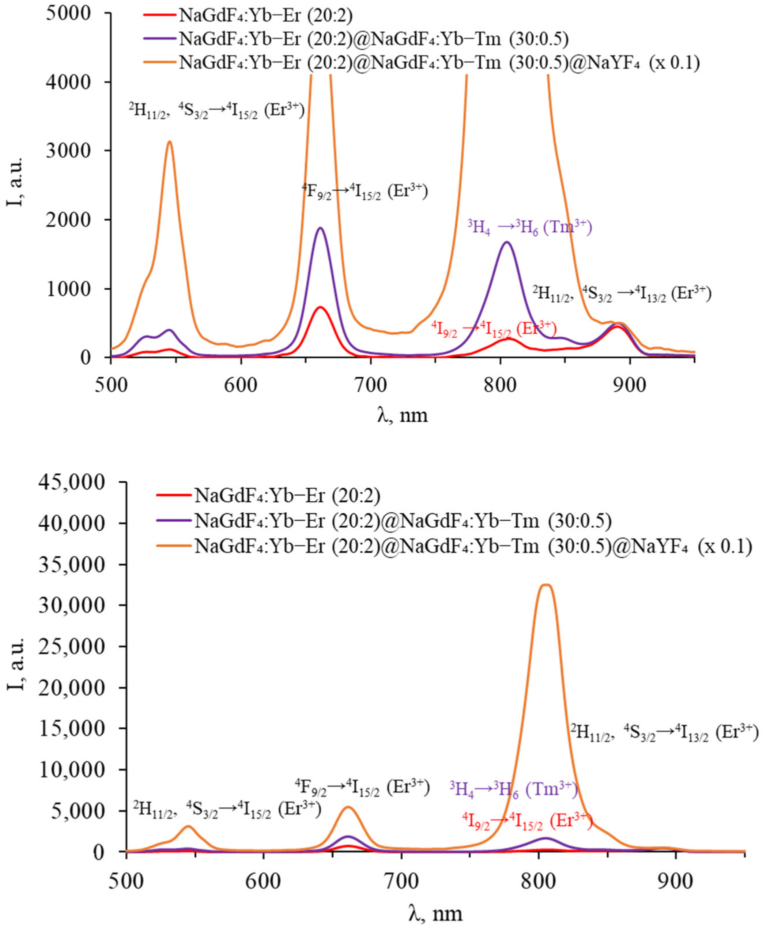

Figure 9. Luminescence spectra of core–shell β-$NaGdF_4$ ($NaGdF_4$:Yb-Er core covered with first $NaGdF_4$:Yb-Tm shell, covered with inert $NaYF_4$ shell) in the VIS range.

In the luminescence spectra of particles with an erbium-doped core in the SWIR, a characteristic band at 1540 nm was observed. After coating with a thulium-doped shell, the integral intensity of the band decreases, as in the case of triple-doped NPs with an increase in the Tm^{3+} concentration, which is due to the competition between Er^{3+} and Tm^{3+} for energy transfer from Yb^{3+}. There is almost no change in the shape of the spectrum after the growth of the shell with thulium; the luminescence peaks of thulium are still not observed in the SWIR spectra, indicating the energy transfer between the Er^{3+} and Tm^{3+} ions located in adjacent shells.

The core-only NPs in the VIS range exhibited characteristic erbium luminescence peaks in the green ($^2H_{11/2}$, $^4S_{3/2} \rightarrow {}^4I_{15/2}$), red ($^4F_{9/2} \rightarrow {}^4I_{15/2}$), and NIR ($^4I_{9/2} \rightarrow {}^4I_{15/2}$ and $^2H_{11/2}$, $^4S_{3/2} \rightarrow {}^4I_{13/2}$) parts of the spectrum. After coating with a thulium shell, an increase in the intensity of the erbium bands is observed in the spectrum of the particles, presumably due to the additional shell protecting erbium ions from surface quenching. A thulium luminescence peak at about 800 nm ($^3H_4 \rightarrow {}^3H_6$) was also present. The intensity of all peaks was increased by coating the NPs with an inert shell.

Spectra recorded for NPs with a Tm^{3+} doped core covered by an Er^{3+} doped shell, in the SWIR and in the VIS range, are shown in Figures 10 and 11, respectively.

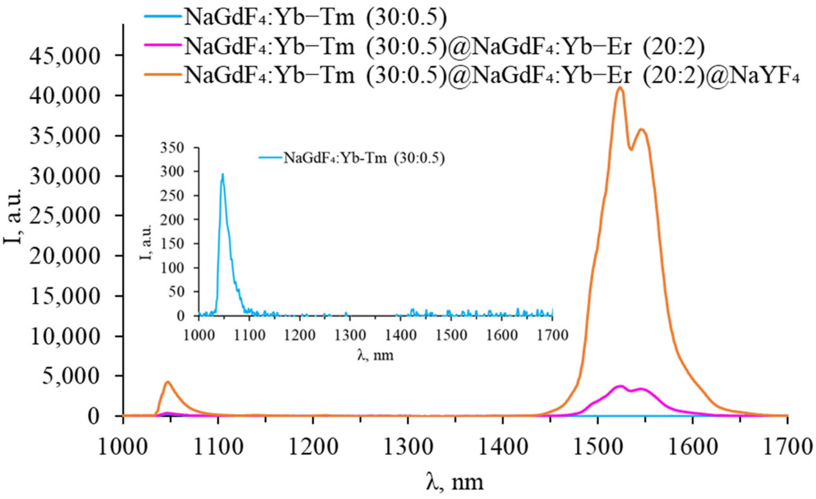

Figure 10. Luminescence spectra of core–shell β-$NaGdF_4$ ($NaGdF_4$:Yb-Tm core covered with first $NaGdF_4$:Yb-Er shell, covered with inert $NaYF_4$ shell) in the SWIR range.

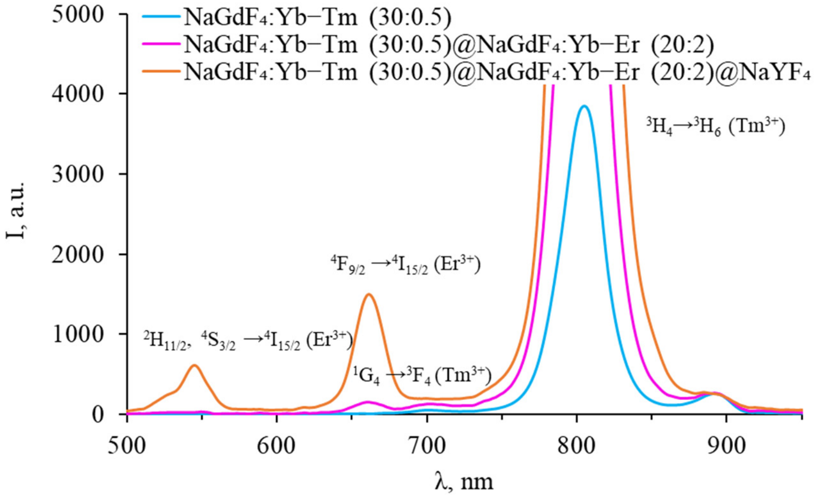

Figure 11. Luminescence spectra of core–shell β-$NaGdF_4$ ($NaGdF_4$:Yb-Tm core covered with first $NaGdF_4$:Yb-Er shell, covered with inert $NaYF_4$ shell) in the VIS range.

No signal was observed in the SWIR spectra of core-only β-$NaGdF_4$:Yb-Tm NPs, but a peak corresponding to the $^3H_4 \rightarrow {}^3H_6$ transition was observed in the VIS range. After coating the particles with an erbium-doped shell, the intensity of this peak increases, while the typical peaks of thulium in the SWIR range are still not observed. The erbium-doped shell prevents the quenching of the thulium luminescence, while the erbium ions themselves remained optically inactive in the VIS range. An erbium luminescence band was observed in the SWIR range at a wavelength of 1540 nm. After coating the particles with an inert shell, erbium luminescence peaks appear in the green and red parts of the spectrum. Thus, the absence of thulium luminescence in the SWIR range can be attributed to the interaction of ions in adjacent shells and/or penetration of rare-earth ions into adjacent shells during the NPs synthesis.

To separate Er^{3+} and Tm^{3+} ions and prevent energy transfer between them, particles with an inert intermediate shell were synthesized: β-$NaGdF_4$:Yb-Tm core covered with a first inert $NaYF_4$ shell (intermediate shell), covered with a $NaGdF_4$:Yb-Er shell, and finally covered with a second inert $NaYF_4$ shell. Spectra in the SWIR and VIS ranges are shown in Figures 12 and 13, respectively.

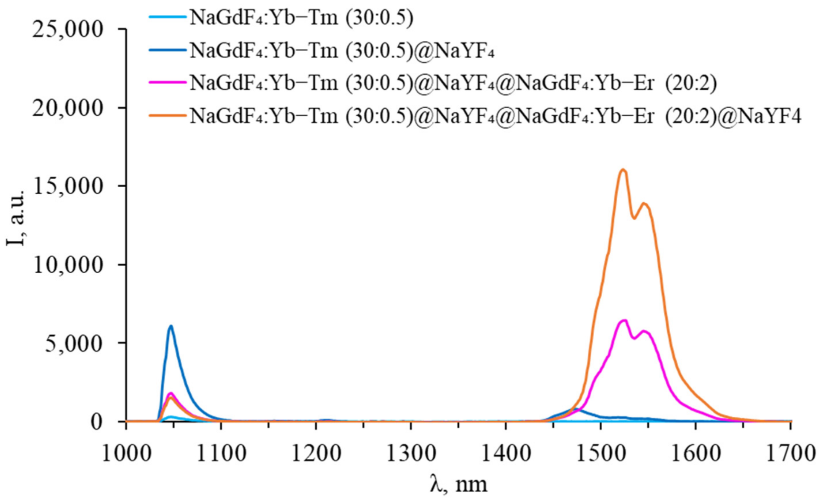

Figure 12. Luminescence spectra of core–shell β-$NaGdF_4$ ($NaGdF_4$:Yb-Tm core covered with first inert $NaYF_4$ shell (intermediate shell), covered with $NaGdF_4$:Yb-Er shell, and covered with second inert $NaYF_4$ shell) in the SWIR range.

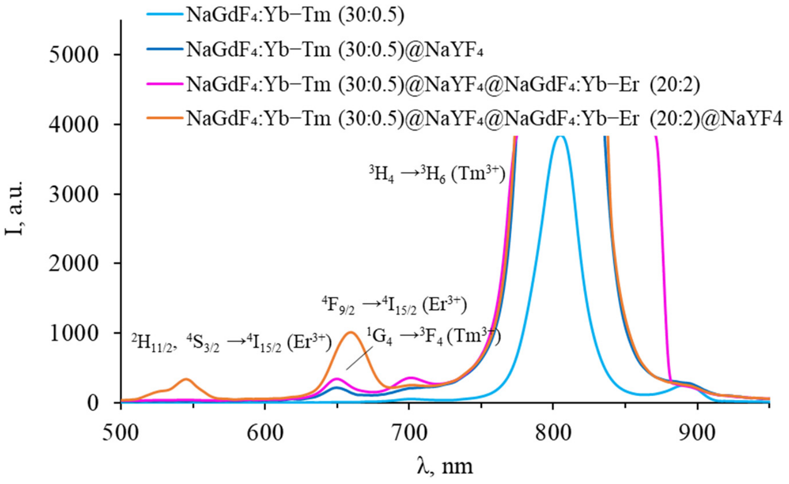

Figure 13. Luminescence spectra of core–shell β-$NaGdF_4$ ($NaGdF_4$:Yb-Tm core covered with first inert $NaYF_4$ shell (intermediate shell), covered with $NaGdF_4$:Yb-Er shell, and covered with second inert $NaYF_4$ shell) in the VIS range.

After coating thulium-doped NPs with an inert shell, the intensity of thulium luminescence in the VIS region increased, and an additional peak corresponding to the $^1G_4 \rightarrow {}^3F_4$ transition appeared. A characteristic peak at 1450 nm appeared in the SWIR range, corresponding to the $^3H_4 \rightarrow {}^3F_4$ transition. This indicates that surface quenching was observed for the luminescence from $^3H_4$ level for uncoated particles. After coating with erbium-doped shell, the peak at 1450 nm disappears, an increase in the intensity of the peaks in the VIS range was observed, while there are no erbium peaks in the VIS range. The erbium shell prevents surface quenching of thulium, while the erbium ions themselves remain optically inactive in the VIS range. However, the thulium luminescence peak in the SWIR range disappeared completely, leaving only the characteristic erbium luminescence peak at 1540 nm. Coating NPs with an inert shell leads to the appearance of additional erbium peaks in the VIS range, an increase in the intensity of erbium luminescence in the SWIR range, and a decrease in the Tm^{3+} luminescence intensity at 800 nm. This suggests that after coating NPs with a final inert shell, erbium ions become optically active, while the role of energy transfer between $Tm^{3+}\,{}^3F_4 \rightarrow {}^3H_6$ and $Er^{3+}\,{}^4I_{13/2} \rightarrow {}^4I_{9/2}$ increases. The upconversion luminescence efficiency for all studied Yb-Er-Tm tri-doped β-$NaGdF_4$ nanoparticles, calculated for the visible range, is presented in Table S1, Supplementary Materials.

3.2.2. Luminescence Lifetime in VIS Range Analysis

To confirm the presence of energy transfer between Tm^{3+} and Er^{3+} active ions, we studied the luminescence lifetime for synthesized samples. The measured decay curves for $Er^{3+}\,{}^2H_{11/2}, {}^4S_{3/2} \rightarrow {}^4I_{15/2}$ (510–550 nm), $^4F_{9/2} \rightarrow {}^4I_{15/2}$ (650–670 nm) transitions and $Tm^{3+}\,{}^1G_4 \rightarrow {}^3F_4$ (640–650 nm) transition are shown in Figure 14.

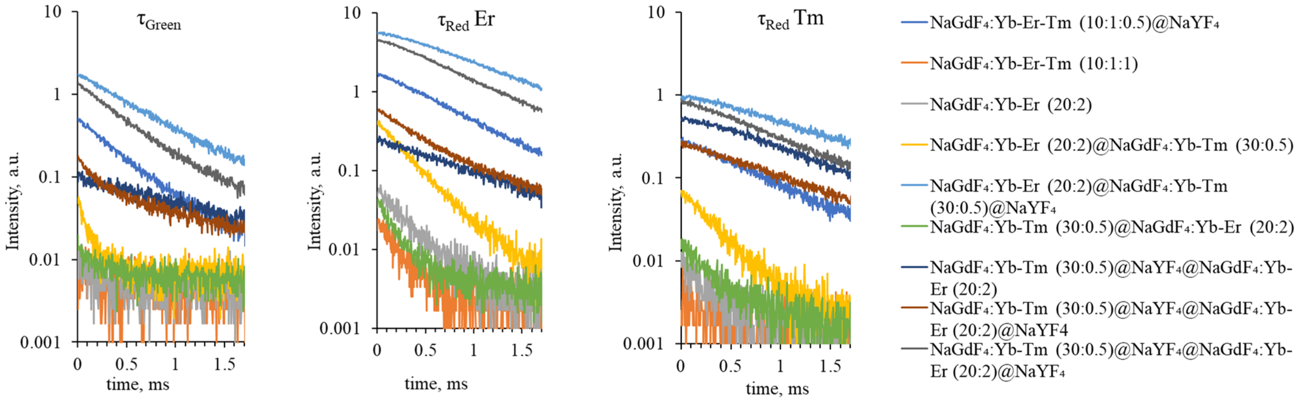

(**a**) (**b**) (**c**)

Figure 14. Upconversion luminescence decay curves for (**a**) $Er^{3+}\,{}^2H_{11/2}, {}^4S_{3/2} \rightarrow {}^4I_{15/2}$ (τ_{green}, 510–550 nm), (**b**) $^4F_{9/2} \rightarrow {}^4I_{15/2}$ (τ_{red} Er, 650–670 nm), and (**c**) $Tm^{3+}\,{}^1G_4 \rightarrow {}^3F_4$ (τ_{red} Tm, 640–650 nm) transitions.

The calculated luminescence lifetime values are presented in Table 2.

For tri-doped NPs, no single peak was observed in the Tm^{3+} luminescence region; the lifetime calculated for the 640–650 nm range corresponds to Er^{3+} red luminescence lifetime (0.210 ± 0.037 ms and 0.221 ± 0.009 ms, respectively). After inert $NaYF_4$ shell coating, the luminescence lifetimes for green and red emission increased up to four times, indicating that the surface quenching is reduced by the $NaYF_4$ shell because the inert shell inhibited surface quenching.

Table 2. Calculated luminescence lifetime for Er^{3+} $^{2}H_{11/2}$, $^{4}S_{3/2}$ → $^{4}I_{15/2}$ (τ_{green}, 510–550 nm), $^{4}F_{9/2}$ → $^{4}I_{15/2}$ (τ_{red} Er, 650–670 nm) transitions and Tm^{3+} $^{1}G_{4}$ → $^{3}F_{4}$ (τ_{red} Tm, 640–650 nm) transition. NA indicates that no single peak was observed in this range; the value in brackets shows the lifetime calculated for this wavelength range.

NPs		**τ_{green}, ms**	**τ_{red} Er, ms**	**τ_{red} Tm, ms**
tri-doped NPs	NaGdF$_4$:Yb-Er-Tm (10:1:0.5)@NaYF$_4$	0.414 ± 0.004	0.735 ± 0.009	NA (0.814 ± 0.019)
	NaGdF$_4$:Yb-Er-Tm (10:1:1)	0.191 ± 0.057	0.221 ± 0.009	NA (0.210 ± 0.037)
Yb-Er core, Yb-Tm shell	NaGdF$_4$:Yb-Er (20:2)	0.120 ± 0.023	0.304 ± 0.008	NA (0.296 ± 0.023)
	NaGdF$_4$:Yb-Er (20:2)@ NaGdF$_4$:Yb-Tm (30:0.5)	0.090 ± 0.003	0.318 ± 0.003	NA (0.333 ± 0.006)
	NaGdF$_4$:Yb-Er (20:2)@ NaGdF$_4$:Yb-Tm (30:0.5)@ NaYF$_4$	0.616 ± 0.006	1.070 ± 0.024	NA (1.292 ± 0.058)
Yb-Tm core, Yb-Er shell	NaGdF$_4$:Yb-Tm (30:0.5)@ NaGdF$_4$:Yb-Er (20:2)	0.231 ± 0.024	0.190 ± 0.004	NA (0.305 ± 0.013)
	NaGdF$_4$:Yb-Tm (30:0.5)@ NaGdF$_4$:Yb-Er (20:2)@NaYF$_4$	0.449 ± 0.003	0.835 ± 0.011	NA (0.953 ± 0.020)
	NaGdF$_4$:Yb-Tm (30:0.5)@ NaYF$_4$@NaGdF$_4$:Yb-Er (20:2)	NA (1.260 ± 0.120)	NA (1.060 ± 0.042)	1.139 ± 0.047
	NaGdF$_4$:Yb-Tm (30:0.5)@ NaYF$_4$@NaGdF$_4$:Yb-Er (20:2)@NaYF$_4$	0.324 ± 0.007	0.498 ± 0.005	1.078 ± 0.036

For NPs with Tm^{3+} and Er^{3+} ions separated in the core and the shell, respectively, we have observed the decrease of Tm^{3+} luminescence intensity in the SWIR range and the reduction of luminescence lifetime upon Er^{3+} doping in the shell.

For the β-NaGdF$_4$:Yb-Tm (30:0.5)@NaGdF$_4$:Yb-Er (20:2)@NaYF$_4$ sample without an inert shell, the thulium luminescence lifetime was estimated to be 0.953 ± 0.020 ms and that of erbium was 0.449 ± 0.003 ms and 0.835 ± 0.011 ms for the green and red regions, respectively. When an intermediate shell is present, the lifetime of thulium increases to 1.078 ± 0.036 ms, while the lifetime of erbium decreases to 0.324 ± 0.007 in the green range and to 0.498 ± 0.005 ms in the red range. However, the lifetime of thulium does not reach the 1.139 ± 0.047 ms registered for β-NaGdF$_4$:Yb-Tm (30:0.5)@NaYF$_4$@NaGdF$_4$:Yb-Er (20:2) composition. We assume that this is because when the shell with Yb-Er is covered with an inert shell, the erbium ions become active and participate in the energy transfer. If there is no inert shell and the erbium shell is exposed, the erbium ions are quenched as a result of interaction with the environment and surface defects (confirmed by the absence of erbium luminescence peaks for β-NaGdF$_4$:Yb-Tm (30:0.5)@NaYF$_4$@NaGdF$_4$:Yb-Er (20:2)).

4. Conclusions

The tri-doped and core–shell single low-temperature hexagonal phase β-NaGdF$_4$ NPs with rare earth ions Yb^{3+}, Er^{3+}, and Tm^{3+} were synthesized. According to TEM data, the samples consisted of particles with semi-spherical morphology. The size of core-only β-NaGdF$_4$:Yb-Tm(30:0.5) NPs ranged from 15 to 40 nm. After shell synthesis, an increase in particle size was observed for both β-NaGdF$_4$:Yb-Er(20:2) and NaYF$_4$ shell, with a shell thickness of about 5 nm.

The lattice parameters of the samples are strongly influenced by the chemical composition of the outer shell. Samples with a NaGdF$_4$-based outer shell have similar lattice parameters. Upon synthesis of a NaYF$_4$ shell, a decrease in lattice parameters was observed, which can be attributed to the smaller size of yttrium cations compared to gadolinium cations.

The coherent scattering region increased in size after the synthesis of each subsequent shell and reached its maximum value for the β-$NaGdF_4$:Yb-Tm(30:0.5)@ $NaYF_4$@$NaGdF_4$:Yb-Er(20:2)@$NaYF_4$ sample. This suggests that particle growth occurred through a classical crystallization mechanism, where the initial core reacted with appropriate oleates, NaOH and NH_4F from the liquid medium. Finally, defectiveness of the core surface decreases, the crystallinity of the nanoparticle improves, and the coherent scattering region increases.

The energy transfer processes in β-$NaGdF_4$:Yb-Er-Tm NPs and core–shell structures were analyzed. No characteristic Tm^{3+} luminescence peaks were observed in the SWIR range for tri-doped NPs. However, the spectra in the VIS range exhibit bands characteristic of both Er^{3+} and Tm^{3+}, which confirms the successful doping of the studied NPs with Tm^{3+}. Since Yb^{3+}-Er^{3+} energy transfer is resonant, while Yb^{3+}-Tm^{3+} energy transfer is non-resonant, transfer to Er^{3+} is more likely.

For core–shell NPs, when Tm^{3+} and Er^{3+} are separated into adjacent layers, quenching cannot be avoided, which is probably due to the mutual diffusion of ions during shell synthesis. For β-$NaGdF_4$:Yb-Er(20:2)@$NaGdF_4$:Yb-Tm(30:0.5)@$NaYF_4$ and β-$NaGdF_4$:Yb-Tm(30:0.5)@$NaGdF_4$:Yb-Er(20:2)@$NaYF_4$, luminescence of thulium could not be registered in the SWIR region.

The use of an inert intermediate $NaYF_4$ shell between the layers containing Tm^{3+} and Er^{3+} was necessary to clearly detect the Tm^{3+} SWIR luminescence in the β-$NaGdF_4$:Yb-Tm (30:0.5)@$NaYF_4$ sample and to partially prevent energy transfer. Without an inert shell for the β-$NaGdF_4$:Yb-Tm(30:0.5)@$NaGdF_4$:Yb-Er(20:2)@$NaYF_4$ sample, the thulium luminescence lifetime was estimated to be 0.953 ± 0.020 ms, while erbium luminescence lifetime was estimated to be 0.449 ± 0.003 ms and 0.835 ± 0.011 ms for the green and red ranges, respectively. When using an intermediate shell, the lifetime of thulium increased to 1.078 ± 0.036 ms, while the lifetime of erbium decreased to 0.324 ± 0.007 ms in the green region and to 0.498 ± 0.005 ms in the red region. However, the lifetime of thulium does not reach the 1.139 ± 0.047 ms registered for β-$NaGdF_4$:Yb-Tm(30:0.5)@$NaYF_4$@$NaGdF_4$:Yb-Er(20:2) composition. After coating the β-$NaGdF_4$:Yb-Tm(30:0.5)@$NaYF_4$ particles with an erbium-doped shell, the thulium luminescence in the SWIR range becomes indistinguishable.

Thus, the use of the core–shell structure does not prevent the energy transfer between ions in adjacent shells. The use of an inert intermediate shell prevents interaction, but only partially, which is probably due to the mutual diffusion of ions during shell synthesis.

Supplementary Materials: The following supporting information can be downloaded at: https://www.mdpi.com/article/10.3390/photonics11010038/s1, Table S1: upconversion luminescence efficiency for Yb-Er-Tm tri-doped β-$NaGdF_4$ nanoparticles, calculated for the visible range. Ref. [67] has been cited in Supplementary Materials.

Author Contributions: Conceptualization, D.P., S.K. and V.P.; methodology, A.R., I.R., D.P., V.P., N.T., S.K. and K.L.; synthesis, V.P.; validation, S.K., V.P., I.R., A.R. and D.P.; formal analysis, D.P., V.P., S.K., N.T. and I.R.; investigation, D.P., V.P. and I.R.; resources, S.K., N.T., D.P. and K.L.; software data processing, I.R., V.P. and K.L.; writing—original draft preparation, D.P.; writing—review and editing, A.R., I.R., S.K., V.P. and D.P.; project administration and funding acquisition, D.P. All authors have read and agreed to the published version of the manuscript.

Funding: This research was funded by a grant from the President of the Russian Federation MK-3098.2022.1.2.

Institutional Review Board Statement: Not applicable.

Informed Consent Statement: Not applicable.

Data Availability Statement: The data presented in this study are available upon request from the corresponding author.

Conflicts of Interest: The authors declare no conflict of interest.

References

1. Mandl, G.A.; Cooper, D.R.; Hirsch, T.; Seuntjens, J.; Capobianco, J.A. Perspective: Lanthanide-Doped Upconverting Nanoparticles. *Methods Appl. Fluoresc.* **2019**, *7*, 012004. [CrossRef]
2. Chen, B.; Wang, F. Emerging Frontiers of Upconversion Nanoparticles. *Trends Chem.* **2020**, *2*, 427–439. [CrossRef]
3. Liang, G.; Wang, H.; Shi, H.; Wang, H.; Zhu, M.; Jing, A.; Li, J.; Li, G. Recent Progress in the Development of Upconversion Nanomaterials in Bioimaging and Disease Treatment. *J. Nanobiotechnol.* **2020**, *18*, 154. [CrossRef] [PubMed]
4. Mettenbrink, E.M.; Yang, W.; Wilhelm, S. Bioimaging with Upconversion Nanoparticles. *Adv. Photonics Res.* **2022**, *3*, 2200098. [CrossRef] [PubMed]
5. Zhao, J.; Jin, D.; Schartner, E.P.; Lu, Y.; Liu, Y.; Zvyagin, A.V.; Zhang, L.; Dawes, J.M.; Xi, P.; Piper, J.A.; et al. Single-Nanocrystal Sensitivity Achieved by Enhanced Upconversion Luminescence. *Nat. Nanotechnol.* **2013**, *8*, 729–734. [CrossRef] [PubMed]
6. Xu, F.; Sun, Y.; Gao, H.; Jin, S.; Zhang, Z.; Zhang, H.; Pan, G.; Kang, M.; Ma, X.; Mao, Y. High-Performance Perovskite Solar Cells Based on NaCsWO$_3$@ NaYF $_4$@NaYF$_4$:Yb,Er Upconversion Nanoparticles. *ACS Appl. Mater. Interfaces* **2021**, *13*, 2674–2684. [CrossRef] [PubMed]
7. Singh, R.; Madirov, E.; Busko, D.; Hossain, I.M.; Konyushkin, V.A.; Nakladov, A.N.; Kuznetsov, S.V.; Farooq, A.; Gharibzadeh, S.; Paetzold, U.W.; et al. Harvesting Sub-Bandgap Photons via Upconversion for Perovskite Solar Cells. *ACS Appl. Mater. Interfaces* **2021**, *13*, 54874–54883. [CrossRef] [PubMed]
8. Del Barrio, M.; Cases, R.; Cebolla, V.; Hirsch, T.; De Marcos, S.; Wilhelm, S.; Galbán, J. A Reagentless Enzymatic Fluorescent Biosensor for Glucose Based on Upconverting Glasses, as Excitation Source, and Chemically Modified Glucose Oxidase. *Talanta* **2016**, *160*, 586–591. [CrossRef]
9. Del Barrio, M.; De Marcos, S.; Cebolla, V.; Heiland, J.; Wilhelm, S.; Hirsch, T.; Galbán, J. Enzyme-Induced Modulation of the Emission of Upconverting Nanoparticles: Towards a New Sensing Scheme for Glucose. *Biosens. Bioelectron.* **2014**, *59*, 14–20. [CrossRef]
10. Radunz, S.; Andresen, E.; Würth, C.; Koerdt, A.; Tschiche, H.R.; Resch-Genger, U. Simple Self-Referenced Luminescent pH Sensors Based on Upconversion Nanocrystals and pH-Sensitive Fluorescent BODIPY Dyes. *Anal. Chem.* **2019**, *91*, 7756–7764. [CrossRef]
11. Wilhelm, S.; Del Barrio, M.; Heiland, J.; Himmelstoß, S.F.; Galbán, J.; Wolfbeis, O.S.; Hirsch, T. Spectrally Matched Upconverting Luminescent Nanoparticles for Monitoring Enzymatic Reactions. *ACS Appl. Mater. Interfaces* **2014**, *6*, 15427–15433. [CrossRef] [PubMed]
12. Xu, M.; Zou, X.; Su, Q.; Yuan, W.; Cao, C.; Wang, Q.; Zhu, X.; Feng, W.; Li, F. Ratiometric Nanothermometer In Vivo Based on Triplet Sensitized Upconversion. *Nat. Commun.* **2018**, *9*, 2698. [CrossRef] [PubMed]
13. Jaque, D.; Vetrone, F. Luminescence Nanothermometry. *Nanoscale* **2012**, *4*, 4301. [CrossRef] [PubMed]
14. Zuo, J.; Tu, L.; Li, Q.; Feng, Y.; Que, I.; Zhang, Y.; Liu, X.; Xue, B.; Cruz, L.J.; Chang, Y.; et al. Near Infrared Light Sensitive Ultraviolet–Blue Nanophotoswitch for Imaging-Guided "Off–On" Therapy. *ACS Nano* **2018**, *12*, 3217–3225. [CrossRef] [PubMed]
15. Li, Y.; Chen, G. Upconversion Nanoparticles for Cancer Therapy. *Adv. NanoBiomed Res.* **2022**, *2*, 2200092. [CrossRef]
16. Suo, H.; Zhu, Q.; Zhang, X.; Chen, B.; Chen, J.; Wang, F. High-Security Anti-Counterfeiting through Upconversion Luminescence. *Mater. Today Phys.* **2021**, *21*, 100520. [CrossRef]
17. Li, Y.; Chen, C.; Liu, F.; Liu, J. Engineered Lanthanide-Doped Upconversion Nanoparticles for Biosensing and Bioimaging Application. *Microchim. Acta* **2022**, *189*, 109. [CrossRef]
18. Auzel, F. Upconversion and Anti-Stokes Processes with f and d Ions in Solids. *Chem. Rev.* **2004**, *104*, 139–174. [CrossRef]
19. Liu, Q.; Sun, Y.; Yang, T.; Feng, W.; Li, C.; Li, F. Sub-10 Nm Hexagonal Lanthanide-Doped NaLuF$_4$ Upconversion Nanocrystals for Sensitive Bioimaging In Vivo. *J. Am. Chem. Soc.* **2011**, *133*, 17122–17125. [CrossRef]
20. Chen, G.; Shen, J.; Ohulchanskyy, T.Y.; Patel, N.J.; Kutikov, A.; Li, Z.; Song, J.; Pandey, R.K.; Ågren, H.; Prasad, P.N.; et al. (α-NaYbF$_4$:Tm^{3+})/CaF$_2$ Core/Shell Nanoparticles with Efficient Near-Infrared to Near-Infrared Upconversion for High-Contrast Deep Tissue Bioimaging. *ACS Nano* **2012**, *6*, 8280–8287. [CrossRef]
21. Tessitore, G.; Mandl, G.A.; Brik, M.G.; Park, W.; Capobianco, J.A. Recent Insights into Upconverting Nanoparticles: Spectroscopy, Modeling, and Routes to Improved Luminescence. *Nanoscale* **2019**, *11*, 12015–12029. [CrossRef] [PubMed]
22. Gao, X.; Cui, Y.; Levenson, R.M.; Chung, L.W.K.; Nie, S. In Vivo Cancer Targeting and Imaging with Semiconductor Quantum Dots. *Nat. Biotechnol.* **2004**, *22*, 969–976. [CrossRef] [PubMed]
23. Lim, Y.T.; Kim, S.; Nakayama, A.; Stott, N.E.; Bawendi, M.G.; Frangioni, J.V. Selection of Quantum Dot Wavelengths for Biomedical Assays and Imaging. *Mol. Imaging* **2003**, *2*, 50–64. [CrossRef] [PubMed]
24. Hemmer, E.; Venkatachalam, N.; Hyodo, H.; Hattori, A.; Ebina, Y.; Kishimoto, H.; Soga, K. Upconverting and NIR Emitting Rare Earth Based Nanostructures for NIR-Bioimaging. *Nanoscale* **2013**, *5*, 11339. [CrossRef] [PubMed]
25. Skripka, A.; Benayas, A.; Marin, R.; Canton, P.; Hemmer, E.; Vetrone, F. Double Rare-Earth Nanothermometer in Aqueous Media: Opening the Third Optical Transparency Window to Temperature Sensing. *Nanoscale* **2017**, *9*, 3079–3085. [CrossRef] [PubMed]
26. Hemmer, E.; Benayas, A.; Légaré, F.; Vetrone, F. Exploiting the Biological Windows: Current Perspectives on Fluorescent Bioprobes Emitting above 1000 Nm. *Nanoscale Horiz.* **2016**, *1*, 168–184. [CrossRef] [PubMed]
27. Smith, A.M.; Mancini, M.C.; Nie, S. Second Window for In Vivo Imaging. *Nat. Nanotechnol.* **2009**, *4*, 710–711. [CrossRef]

28. Ma, D.; Xu, X.; Hu, M.; Wang, J.; Zhang, Z.; Yang, J.; Meng, L. Rare-Earth-Based Nanoparticles with Simultaneously Enhanced Near-Infrared (NIR)-Visible (Vis) and NIR-NIR Dual-Conversion Luminescence for Multimodal Imaging. *Chem. Asian J.* **2016**, *11*, 1050–1058. [CrossRef]
29. Chang, Y.; Chen, H.; Xie, X.; Wan, Y.; Li, Q.; Wu, F.; Yang, R.; Wang, W.; Kong, X. Bright Tm^{3+}-Based Downshifting Luminescence Nanoprobe Operating around 1800 Nm for NIR-IIb and c Bioimaging. *Nat. Commun.* **2023**, *14*, 1079. [CrossRef]
30. Wang, L.; Yan, R.; Huo, Z.; Wang, L.; Zeng, J.; Bao, J.; Wang, X.; Peng, Q.; Li, Y. Fluorescence Resonant Energy Transfer Biosensor Based on Upconversion-Luminescent Nanoparticles. *Angew. Chem. Int. Ed.* **2005**, *44*, 6054–6057. [CrossRef]
31. Kamimura, M.; Matsumoto, T.; Suyari, S.; Umezawa, M.; Soga, K. Ratiometric Near-Infrared Fluorescence Nanothermometry in the OTN-NIR (NIR II/III) Biological Window Based on Rare-Earth Doped β-$NaYF_4$ Nanoparticles. *J. Mater. Chem. B* **2017**, *5*, 1917–1925. [CrossRef] [PubMed]
32. Naczynski, D.J.; Tan, M.C.; Zevon, M.; Wall, B.; Kohl, J.; Kulesa, A.; Chen, S.; Roth, C.M.; Riman, R.E.; Moghe, P.V. Rare-Earth-Doped Biological Composites as In Vivo Shortwave Infrared Reporters. *Nat. Commun.* **2013**, *4*, 2199. [CrossRef] [PubMed]
33. Sekiyama, S.; Umezawa, M.; Kuraoka, S.; Ube, T.; Kamimura, M.; Soga, K. Temperature Sensing of Deep Abdominal Region in Mice by Using over-1000 Nm Near-Infrared Luminescence of Rare-Earth-Doped $NaYF_4$ Nanothermometer. *Sci. Rep.* **2018**, *8*, 16979. [CrossRef] [PubMed]
34. Wortmann, L.; Suyari, S.; Ube, T.; Kamimura, M.; Soga, K. Tuning the Thermal Sensitivity of β-NaYF4: Yb^{3+}, Ho^{3+}, Er^{3+} Nanothermometers for Optimal Temperature Sensing in OTN-NIR (NIR II/III) Biological Window. *J. Lumin.* **2018**, *198*, 236–242. [CrossRef]
35. Ximendes, E.C.; Rocha, U.; Sales, T.O.; Fernández, N.; Sanz-Rodríguez, F.; Martín, I.R.; Jacinto, C.; Jaque, D. In Vivo Subcutaneous Thermal Video Recording by Supersensitive Infrared Nanothermometers. *Adv. Funct. Mater.* **2017**, *27*, 1702249. [CrossRef]
36. Cortelletti, P.; Skripka, A.; Facciotti, C.; Pedroni, M.; Caputo, G.; Pinna, N.; Quintanilla, M.; Benayas, A.; Vetrone, F.; Speghini, A. Tuning the Sensitivity of Lanthanide-Activated NIR Nanothermometers in the Biological Windows. *Nanoscale* **2018**, *10*, 2568–2576. [CrossRef] [PubMed]
37. Xia, H.; Lei, L.; Xia, J.; Hua, Y.; Deng, D.; Xu, S. Yb/Er/Tm Tri-Doped Na3ZrF7 Upconversion Nanocrystals for High Performance Temperature Sensing. *J. Lumin.* **2019**, *209*, 8–13. [CrossRef]
38. Li, J.; Wang, Y.; Zhang, X.; Li, L.; Hao, H. Up-Converting Luminescence and Temperature Sensing of $Er^{3+}/Tm^{3+}/Yb^{3+}$ Co-Doped NaYF4 Phosphors Operating in Visible and the First Biological Window Range. *Nanomaterials* **2021**, *11*, 2660. [CrossRef]
39. Yang, J.; Zhang, C.; Peng, C.; Li, C.; Wang, L.; Chai, R.; Lin, J. Controllable Red, Green, Blue (RGB) and Bright White Upconversion Luminescence of Lu_2 O_3:$Yb^{3+}/Er^{3+}/Tm^{3+}$ Nanocrystals through Single Laser Excitation at 980 Nm. *Chem. Eur. J.* **2009**, *15*, 4649–4655. [CrossRef]
40. Liu, Y.; Xu, C.; Yang, Q. White Upconversion of Rare-Earth Doped ZnO Nanocrystals and Its Dependence on Size of Crystal Particles and Content of Yb^{3+} and Tm^{3+}. *J. Appl. Phys.* **2009**, *105*, 084701. [CrossRef]
41. Ray, S.K.; Joshi, B.; Hur, J. White-Light Emission in $Yb^{3+}/Er^{3+}/Tm^{3+}$- and $Yb^{3+}/Er^{3+}/Tm^{3+}$ /Ho^{3+}-Doped α-$NiMoO_4$ Nanoparticles. *Nanotechnology* **2022**, *33*, 395705. [CrossRef] [PubMed]
42. Pominova, D.; Proydakova, V.; Romanishkin, I.; Ryabova, A.; Kuznetsov, S.; Uvarov, O.; Fedorov, P.; Loschenov, V. Temperature Sensing in the Short-Wave Infrared Spectral Region Using Core-Shell $NaGdF_4$:Yb^{3+}, Ho^{3+}, Er^{3+}@$NaYF_4$ Nanothermometers. *Nanomaterials* **2020**, *10*, 1992. [CrossRef] [PubMed]
43. Zhou, J.; Liu, Q.; Feng, W.; Sun, Y.; Li, F. Upconversion Luminescent Materials: Advances and Applications. *Chem. Rev.* **2015**, *115*, 395–465. [CrossRef] [PubMed]
44. Chen, G.; Ågren, H.; Ohulchanskyy, T.Y.; Prasad, P.N. Light Upconverting Core–Shell Nanostructures: Nanophotonic Control for Emerging Applications. *Chem. Soc. Rev.* **2015**, *44*, 1680–1713. [CrossRef] [PubMed]
45. Han, S.; Deng, R.; Xie, X.; Liu, X. Enhancing Luminescence in Lanthanide-Doped Upconversion Nanoparticles. *Angew. Chem. Int. Ed.* **2014**, *53*, 11702–11715. [CrossRef] [PubMed]
46. Fisher, J.; Zhao, B.; Lin, C.; Berry, M.; May, P.S.; Smith, S. Spectroscopic Imaging and Power Dependence of Near-Infrared to Visible Upconversion Luminescence from $NaYF_4$:Yb^{3+}, Er^{3+} Nanoparticles on Nanocavity Arrays. *J. Phys. Chem. C* **2015**, *119*, 24976–24982. [CrossRef]
47. Noculak, A.; Podhorodecki, A. Size and Shape Effects in β-$NaGdF_4$: Yb^{3+}, Er^{3+} Nanocrystals. *Nanotechnology* **2017**, *28*, 175706. [CrossRef]
48. Krämer, K.W.; Biner, D.; Frei, G.; Güdel, H.U.; Hehlen, M.P.; Lüthi, S.R. Hexagonal Sodium Yttrium Fluoride Based Green and Blue Emitting Upconversion Phosphors. *Chem. Mater.* **2004**, *16*, 1244–1251. [CrossRef]
49. Suyver, J.F.; Aebischer, A.; Biner, D.; Gerner, P.; Grimm, J.; Heer, S.; Krämer, K.W.; Reinhard, C.; Güdel, H.U. Novel Materials Doped with Trivalent Lanthanides and Transition Metal Ions Showing Near-Infrared to Visible Photon Upconversion. *Opt. Mater.* **2005**, *27*, 1111–1130. [CrossRef]
50. Niu, N.; He, F.; Gai, S.; Li, C.; Zhang, X.; Huang, S.; Yang, P. Rapid Microwave Reflux Process for the Synthesis of Pure Hexagonal NaYF4:Yb^{3+},Ln^{3+},Bi^{3+} (Ln^{3+} = Er^{3+}, Tm^{3+}, Ho^{3+}) and Its Enhanced UC Luminescence. *J. Mater. Chem.* **2012**, *22*, 21613. [CrossRef]
51. Kumar, V.; Som, S.; Dutta, S.; Das, S.; Swart, H.C. Influence of Ho3+ Doping on the Temperature Sensing Behavior of Er^{3+}-Yb^{3+} Doped La_2CaZnO_5 Phosphor. *RSC Adv.* **2016**, *6*, 84914–84925. [CrossRef]
52. Banski, M.; Podhorodecki, A.; Misiewicz, J.; Afzaal, M.; Abdelhady, A.L.; O'Brien, P. Selective Excitation of Eu^{3+} in the Core of Small β-$NaGdF_4$ Nanocrystals. *J. Mater. Chem. C* **2013**, *1*, 801–807. [CrossRef]

53. Dong, H.; Sun, L.-D.; Yan, C.-H. Energy Transfer in Lanthanide Upconversion Studies for Extended Optical Applications. *Chem. Soc. Rev.* **2015**, *44*, 1608–1634. [CrossRef] [PubMed]
54. Chan, E.M.; Levy, E.S.; Cohen, B.E. Rationally Designed Energy Transfer in Upconverting Nanoparticles. *Adv. Mater.* **2015**, *27*, 5753–5761. [CrossRef]
55. Huang, L.; Wang, L.; Xue, X.; Zhao, D.; Qin, G.; Qin, W. Enhanced Red Upconversion Luminescence in Er–Tm Codoped $NaYF_4$ Phosphor. *J. Nanosci. Nanotechnol.* **2011**, *11*, 9498–9501. [CrossRef] [PubMed]
56. Chan, E.M.; Han, G.; Goldberg, J.D.; Gargas, D.J.; Ostrowski, A.D.; Schuck, P.J.; Cohen, B.E.; Milliron, D.J. Combinatorial Discovery of Lanthanide-Doped Nanocrystals with Spectrally Pure Upconverted Emission. *Nano Lett.* **2012**, *12*, 3839–3845. [CrossRef]
57. Chan, E.M.; Gargas, D.J.; Schuck, P.J.; Milliron, D.J. Concentrating and Recycling Energy in Lanthanide Codopants for Efficient and Spectrally Pure Emission: The Case of $NaYF_4$:Er $^{3+}$ /Tm $^{3+}$ Upconverting Nanocrystals. *J. Phys. Chem. B* **2012**, *116*, 10561–10570. [CrossRef]
58. Prorok, K.; Pawlyta, M.; Stręk, W.; Bednarkiewicz, A. Energy Migration Up-Conversion of Tb^{3+} in Yb^{3+} and Nd^{3+} Codoped Active-Core/Active-Shell Colloidal Nanoparticles. *Chem. Mater.* **2016**, *28*, 2295–2300. [CrossRef]
59. Chen, B.; Wang, F. Combating Concentration Quenching in Upconversion Nanoparticles. *Acc. Chem. Res.* **2020**, *53*, 358–367. [CrossRef]
60. Zhang, Y.; Wen, R.; Hu, J.; Guan, D.; Qiu, X.; Zhang, Y.; Kohane, D.S.; Liu, Q. Enhancement of Single Upconversion Nanoparticle Imaging by Topologically Segregated Core-Shell Structure with Inward Energy Migration. *Nat. Commun.* **2022**, *13*, 5927. [CrossRef]
61. Shen, B.; Cheng, S.; Gu, Y.; Ni, D.; Gao, Y.; Su, Q.; Feng, W.; Li, F. Revisiting the Optimized Doping Ratio in Core/Shell Nanostructured Upconversion Particles. *Nanoscale* **2017**, *9*, 1964–1971. [CrossRef]
62. Zhou, B.; Tang, B.; Zhang, C.; Qin, C.; Gu, Z.; Ma, Y.; Zhai, T.; Yao, J. Enhancing Multiphoton Upconversion through Interfacial Energy Transfer in Multilayered Nanoparticles. *Nat. Commun.* **2020**, *11*, 1174. [CrossRef]
63. Pominova, D.V.; Romanishkin, I.D.; Proydakova, V.Y.; Grachev, P.V.; Moskalev, A.S.; Ryabova, A.V.; Makarov, V.I.; Linkov, K.G.; Kuznetsov, S.V.; Voronov, V.V.; et al. Optimization of Upconversion Luminescence Excitation Mode for Deeper In Vivo Bioimaging without Contrast Loss or Overheating. *Methods Appl. Fluoresc.* **2020**, *8*, 025006. [CrossRef]
64. Pominova, D.; Romanishkin, I.; Proydakova, V.; Kuznetsov, S.; Grachev, P.; Ryabova, A.; Tabachkova, N.; Fedorov, P.; Loschenov, V. Study of Synthesis Temperature Effect on β-$NaGdF_4$: Yb^{3+}, Er^{3+} Upconversion Luminescence Efficiency and Decay Time Using Maximum Entropy Method. *Methods Appl. Fluoresc.* **2022**, *10*, 024005. [CrossRef]
65. Pominova, D.V.; Proydakova, V.Y.; Romanishkin, I.D.; Ryabova, A.V.; Grachev, P.V.; Makarov, V.I.; Kuznetsov, S.V.; Uvarov, O.V.; Voronov, V.V.; Yapryntsev, A.D.; et al. Achieving High NIR-to-NIR Conversion Efficiency by Optimization of Tm^{3+} Content in $Na(Gd,Yb)F_4$: Tm Upconversion Luminophores. *Laser Phys. Lett.* **2020**, *17*, 125701. [CrossRef]
66. Shannon, R.D. Revised Effective Ionic Radii and Systematic Studies of Interatomic Distances in Halides and Chalcogenides. *Acta Cryst. A* **1976**, *32*, 751–767. [CrossRef]
67. Ryabova, A.V.; Pominova, D.V.; Krutko, V.A.; Komova, M.G.; Loschenov, V.B. Spectroscopic research of upconversion nanomaterials based on complex oxide compounds doped with rare-earth ion pairs: Benefit for cancer diagnostics by upconversion fluorescence and radio sensitive methods. *Photon. Lasers Med.* **2013**, *2*, 117–128. [CrossRef]